LUND UNIVERSITY

Fisher information analysis for two-dimensional microwave tomography

Nordebo, Sven; Gustafsson, Mats; Nilsson, Börje

2006

[Link to publication](#)

Total number of authors:
3

Fisher Information Analysis for Two-Dimensional Microwave Tomography

Sven Nordebo, Mats Gustafsson, and Börje Nilsson
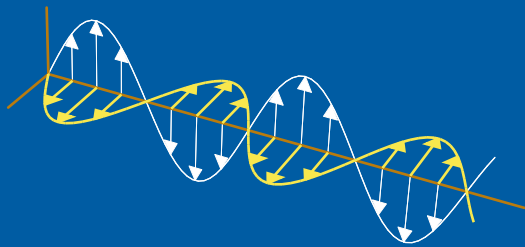
Sven Nordebo
Sven.Nordebo@msi.vxu.se

School of Mathematics and System Engineering
Växjö University
351 95 Växjö
Sweden

Mats Gustafsson
Mats.Gustafsson@es.lth.se

Department of Electroscience
Electromagnetic Theory
P.O. Box 118
SE-221 00 Lund
Sweden

Börje Nilsson
Borje.Nilsson@msi.vxu.se

School of Mathematics and System Engineering
Växjö University
351 95 Växjö
Sweden

Abstract

In this paper, a Fisher information analysis is employed to establish some important physical performance bounds in microwave tomography. As a canonical problem, the two-dimensional electromagnetic inverse problem of imaging a cylinder with isotropic dielectric losses is considered. A fixed resolution is analyzed by introducing a finite basis, *i.e.*, pixels representing the material properties. The corresponding Cramér-Rao bound for estimating the pixel values is computed based on a calculation of the *sensitivity field* which is obtained by differentiating the observed field with respect to the estimated parameter. An optimum trade-off between the accuracy and the resolution is defined based on the Cramér-Rao bound, and its application to asses a practical resolution limit in the inverse problem is discussed. Numerical examples are included to illustrate how the Fisher information analysis can be used to investigate the significance of measurement distance, operating frequency and losses in the canonical tomography set-up.

1 Introduction

Although imaging and inverse scattering problems have been thoroughly studied during the last century there is only a partial understanding of these complex problems. Most of the efforts have been placed on the development of efficient inversion algorithms and mathematical uniqueness results. In comparison, there are very few results and a limited knowledge about the information content in the inversion data. Inverse scattering and imaging are topics with a variety of applications in *e.g.*, medicine, non-destructive testing, surveillance, quantum mechanics, acoustics and optics. These problems are in general ill-posed, *i.e.*, they are not well-posed in the sense of existence, uniqueness, and the solution being a continuous function of the data [1, 5, 9, 11, 13, 15, 25]. The Radon transform inversion used in computerized tomography (CT) is an elegant example of the solution to an ill-posed problem of great importance in industry and medicin [1, 25].

Microwave tomography has several promising applications in *e.g.*, non-invasive medical imaging and early detection of breast tumors [8], and non–destructive testing [3, 9]. Besides the analytical and computational challenges of the inversion algorithms, the basic understanding of the microwave tomography set-up is not adequate. There is a need to improve the understanding of the significance of the number, positions, and radiation patterns of the antennas. The used signal spectrum, the influence of the noise statistics, and partial knowledge of the objects (a priori information) are also very important issues in this respect.

The mathematical theory is well developed concerning the uniqueness of inverse scattering problems [5, 11, 13, 25]. The uniqueness theorems typically show that the solution is unique if the data is available from all possible measurements. This is very important but not sufficient from a practical point of view. Further, since the solution of ill-posed problems does not generally depend continuously on the data, the effect of noise is amplified in a way that calls for proper control. For this purpose, regularization theory [1] is often used to control the imaging error. Typically, the

number of degrees of freedom (NDF) pertaining the number of significant singular values of a linear operator is a very useful tool, see *e.g.*, [1, 2, 22]. The NDF, which is virtually independent of the noise level, can be used to estimate the number of retrievable parameters of an object, and hence the resolution. However, these approaches are rather coarse and do not give a qualitative measure on the information content of the inversion data with respect to the accuracy and the resolution of images. We are seeking a measure that can furnish a deeper understanding about the physics of the measurement problem.

Estimation theory is a classical and well developed area within signal processing research and mathematical statistics. Over several decades the Cramér-Rao bound (CRB) has been subjected to many revivals and has become the dominating tool in areas such as statistical signal processing [12], array signal processing [14] and systems and control theory [24]. Signal models typically rely on certain geometrical assumptions about the wave propagation [14], or a rational or polynomial description of the systems or signals under consideration [24]. However, physically based mathematical models are oftenly not considered even though the signals under consideration are related to physical phenomena. On the other hand, we have also observed that estimation theory such as Fisher information and Bayesian estimation [12], are tools that have not been fully exploited in the traditional inverse scattering or imaging literature. One of the very few overviews on this subject is given in [25].

A Fisher information analysis and the Cramér-Rao bound provides a very useful instrument for sensitivity analysis of various wave propagation phenomena, and which facilitates valuable physical interpretations, see *e.g.*, [4, 6, 7, 10, 17, 20, 21, 23, 26]. Cramér-Rao bounds for the location, size and orientation of a known object has been studied in the context of diffraction tomography and Maximum Likelihood (ML) estimation in [6, 17, 26]. Previously, the Cramér-Rao bound has been employed as an analytical tool to investigate the one-dimensional inverse scattering problem of multilayer structures [10]. The Fisher information analysis has also been used with electromagnetic inverse source problems, see *e.g.*, [20, 21]. In [10, 20, 21], the Cramér-Rao bound is employed as an analytical tool to quantify the ill-posedness of the reconstruction and to explicitly describe the inherent trade-off between the accuracy and the resolution.

The purpose of the present paper is to provide a general framework for sensitivity analysis which is useful for establishing some important physical performance bounds in microwave tomography. As a canonical problem, the two-dimensional electromagnetic inverse problem of imaging a cylinder with isotropic dielectric losses (modelled with a complex valued permittivity) is considered. However, we anticipate that the presented technique can be useful also in more general settings such as with anisotropic material parameters, see *e.g.*, [18, 19]. A fixed resolution is analyzed by introducing a finite basis, *i.e.*, pixels representing the material properties. The corresponding Cramér-Rao bound for estimating the pixel values is computed based on a calculation of the *sensitivity field* which is obtained by differentiating the observed field with respect to the estimated parameter. Here, the resemblance with Fréchet differentials and sensitivity analysis should be observed [25]. For the
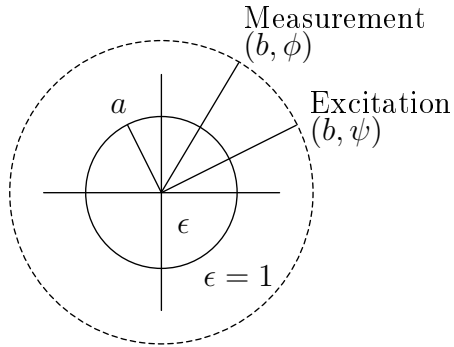
Figure 1: Measurement set-up with a cylindrical object of radius a and relative permittivity ϵ. Measurement cylinder of radius b in free space with excitation at (b, ψ) and measurement at (b, ϕ).

canonical problem, the domain as well as the discrete calculation- and pixel grids are circularly symmetrical. This condition greatly simplifies the interpretation as well as the calculation of the Cramér-Rao bound which is based on the background Greens function. An optimum trade-off between the accuracy and the resolution is defined based on the Cramér-Rao bound, and its application to asses a practical resolution limit in the inverse problem is discussed. Hence, when the resolution of an imaging system is improved, the corresponding estimation accuracy in a given measurement set-up is impaired in the sense that the Cramér-Rao bound is increased. Numerical examples are included to illustrate how the Fisher information analysis can be used to investigate the significance of measurement distance, operating frequency and losses in the canonical tomography set-up.

The rest of the paper is outlined as follows. Section 2 presents the electromagnetic model as well as the statistical model of the canonical problem. Section 3 presents the Fisher information analysis based on the Cramér-Rao bound and a calculation of the sensitivity field using the background Greens function. Section 4 presents the numerical examples and section 5 the summary and conclusions. An appendix is also included defining the circularly symmetrical background Greens function.

2 Measurement model

2.1 Electromagnetic model

Throughout the paper, let (ρ, ϕ, z) denote the cylindrical coordinates, $(\hat{\boldsymbol{\rho}}, \hat{\boldsymbol{\phi}}, \hat{\boldsymbol{z}})$ the corresponding unit vectors and $\boldsymbol{\rho} = \rho\hat{\boldsymbol{\rho}}$ the two-dimensional radius vector with coordinates (ρ, ϕ). We will assume that all fields have a two-dimensional domain and that the electric field $\boldsymbol{E}$ is vertically polarized, hence $\boldsymbol{E} = E(\boldsymbol{\rho})\hat{\boldsymbol{z}}$ where $E(\boldsymbol{\rho})$ is the two-dimensional scalar field depending on the spatial coordinate $\boldsymbol{\rho}$. Further, let $\mathrm{e}^{\mathrm{i}\omega t}$ be the time-convention and let k_0, c and η denote the wave number, the speed of light and the wave impedance of free space, respectively.

We consider the electromagnetic inverse problem of imaging a two-dimensional circular cylinder with isotropic dielectric losses as depicted in Figure 1. The measurement set-up consists of a cylindrical object of radius a and a measurement cylinder of radius b in free space with excitation at (b, ψ) and measurement at (b, ϕ). The inverse problem is to estimate the relative permittivity $\epsilon(\boldsymbol{\rho})$ within the cylinder, based on all measurements of the electric field $E(b, \phi, \psi)$ for $(\phi, \psi) \in [0, 2\pi] \times [0, 2\pi]$.

The electric and magnetic fields $\boldsymbol{E}$ and $\boldsymbol{H}$ satisfy Maxwell's equations

$$\begin{cases} \nabla \times \boldsymbol{E} + \mathrm{i}k_0 \eta \boldsymbol{H} = \boldsymbol{0} \\ \nabla \times \boldsymbol{H} - \mathrm{i}\frac{k_0}{\eta}\epsilon \boldsymbol{E} = \boldsymbol{J}_{\mathrm{s}} \end{cases} \tag{2.1}$$

together with appropriate boundary conditions (see the appendix), and where $\boldsymbol{J}_{\mathrm{s}}$ is the excitation source and ϵ the complex valued relative permittivity of the cylinder.

It is assumed that the background is homogenous and the corresponding permittivity ϵ is known (either modelled or measured) as we analyze the optimum performance of estimating its deviation at a particular background level. A simple conductivity model is to employ a real valued relative permittivity ϵ_∞ (instantaneous response) and a conductivity σ to get $\epsilon = \epsilon_\infty - \mathrm{i}\frac{\sigma}{\omega\epsilon_0}$. More sophisticated models such as the Debye and Lorentz models, or combinations thereof, can be straightforwardly incorporated in the sensitivity analysis below.

Assuming that the source is vertically polarized with $\boldsymbol{J}_{\mathrm{s}} = J\hat{\boldsymbol{z}}$, Maxwell's equations (2.1) yield the following wave equation for the scalar field E

$$\mathcal{L}E = \left\{ \frac{1}{\rho}\frac{\partial}{\partial\rho}\rho\frac{\partial}{\partial\rho} + \frac{1}{\rho^2}\frac{\partial^2}{\partial\phi^2} + k^2 \right\} E = \mathrm{i}k_0 \eta J \tag{2.2}$$

together with appropriate boundary conditions (see the appendix), and where $k^2 = \omega^2 \mu_0 \epsilon_0 \epsilon = k_0^2 \epsilon$. The corresponding Greens function $G(\boldsymbol{\rho}, \boldsymbol{\rho}') = G(\rho, \phi, \rho', \phi')$ for a point source at $\boldsymbol{\rho}' = (\rho', \phi')$ satisfies $\mathcal{L}G(\boldsymbol{\rho}, \boldsymbol{\rho}') = -\delta(\boldsymbol{\rho} - \boldsymbol{\rho}')$ and is given in the appendix for the homogenous and circularly symmetrical background. Assuming that the source is a point source at (b, ψ) and the measurement is performed at (b, ϕ), the observed quantity is hence given by

$$E(b, \phi, \psi) = -\mathrm{i}k_0 \eta G(b, \phi, b, \psi). \tag{2.3}$$

2.2 Statistical model

We now adopt the following statistical measurement model

$$E^{(\mathrm{m})}(b, \phi, \psi) = E(b, \phi, \psi) + N(\phi, \psi) \tag{2.4}$$

where $(\phi, \psi) \in [0, 2\pi] \times [0, 2\pi]$ and $N(\phi, \psi)$ is additive measurement noise. Here, $N(\phi, \psi)$ is modelled as a two-dimensional uncorrelated zero mean complex Gaussian random process [16] with autocorrelation function

$$\mathcal{E}\left\{ N^*(\phi + \Delta\phi, \psi + \Delta\psi)N(\phi, \psi) \right\} = (2\pi)^2 \sigma_{\mathrm{N}}^2 \delta(\Delta\phi, \Delta\psi) \tag{2.5}$$

where $\mathcal{E}\{\cdot\}$ denotes the expectation operator, $(\cdot)^*$ the complex conjugate and $\delta(\cdot)$ the Dirac δ-function (here with period $2\pi \times 2\pi$). The strength of the noise is given by the spatial spectral density σ_N^2.

It is natural to examine the $2\pi \times 2\pi$ periodic function $E(b, \phi, \psi)$ by its two-dimensional Fourier series representation

$$\widetilde{E}_{mn}(b) = \frac{1}{(2\pi)^2} \int_0^{2\pi} \int_0^{2\pi} E(b, \phi, \psi) \mathrm{e}^{-im\phi - in\psi} \, \mathrm{d}\phi \, \mathrm{d}\psi \qquad (2.6)$$

yielding the discrete measurement model

$$\widetilde{E}_{mn}^{(\mathrm{m})}(b) = \widetilde{E}_{mn}(b) + \widetilde{N}_{mn} \qquad (2.7)$$

where the autocorrelation function of the noise is given by

$$\mathcal{E}\left\{\widetilde{N}_{mn}^* \widetilde{N}_{m'n'}\right\} = \sigma_\mathrm{N}^2 \delta_{mm'} \delta_{nn'}, \ -\infty < m, n < \infty \qquad (2.8)$$

and where $\delta_{nn'}$ denotes the Kronecker delta.

Let $\widetilde{G}_m(\rho, \rho', \phi')$ denote the one-dimensional Fourier series representation of the Greens function $G(\rho, \phi, \rho', \phi')$. We have then for the homogenous and circularly symmetrical background that $\widetilde{E}_{mn}(b) = -ik_0\eta\widetilde{G}_m(b, b, 0)\delta_{-m,n}$ since $\widetilde{G}_m(b, b, \psi) = \widetilde{G}_m(b, b, 0)\mathrm{e}^{-im\psi}$, see the appendix. The signal-to-noise ratio is now defined as

$$\mathrm{SNR} = \frac{P_\mathrm{s}(b, k_0)}{\sigma_\mathrm{N}^2} \qquad (2.9)$$

where $P_\mathrm{s}(b, k_0)$ is the average squared signal amplitude

$$P_\mathrm{s}(b, k_0) = \frac{1}{(2\pi)^2} \int_0^{2\pi} \int_0^{2\pi} |E(b, \phi, \psi)|^2 \, \mathrm{d}\phi \, \mathrm{d}\psi$$

$$= \sum_{m=-\infty}^{\infty} \sum_{n=-\infty}^{\infty} |\widetilde{E}_{mn}(b)|^2 = k_0^2\eta^2 \sum_{m=-\infty}^{\infty} |\widetilde{G}_m(b, b, 0)|^2 \quad (2.10)$$

where the average is taken over all measurements with $(\phi, \psi) \in [0, 2\pi] \times [0, 2\pi]$.

3 Fisher Information Analysis

3.1 The Sensitivity Field

Assume that the cylinder region $\mathcal{S} = \cup_{i=1}^I \mathcal{S}_i$ is decomposed into a finite set of disjoint image cells or pixels $\mathcal{S}_i$ corresponding to some specific scale of resolution, see Figure 4 for an example. The complex valued relative permittivity within the cylinder is hence discretized according to the finite expansion

$$\epsilon = \sum_{i=1}^I \epsilon_i \chi_i \qquad (3.1)$$

where ϵ_i are complex parameters and χ_i is the set function for pixel $\mathcal{S}_i$ ($\chi_i(\boldsymbol{\rho}) = 1$ if $\boldsymbol{\rho} \in \mathcal{S}_i$ and $\chi_i(\boldsymbol{\rho}) = 0$ if $\boldsymbol{\rho} \notin \mathcal{S}_i$).

The Fisher information matrix [12] for the parameters ϵ_i based on the statistical measurement model (2.7) is given by

$$\boldsymbol{\mathcal{I}}_{ij} = \frac{1}{\sigma_{\mathrm{N}}^2} \sum_{m=-\infty}^{\infty} \sum_{n=-\infty}^{\infty} \frac{\partial \widetilde{E}_{mn}^*(b)}{\partial \epsilon_i^*} \frac{\partial \widetilde{E}_{mn}(b)}{\partial \epsilon_j}. \tag{3.2}$$

By Parseval's theorem, the Fisher information (3.2) is also given by

$$\boldsymbol{\mathcal{I}}_{ij} = \frac{1}{\sigma_{\mathrm{N}}^2 (2\pi)^2} \int_{-\pi}^{\pi} \int_{-\pi}^{\pi} \frac{\partial E^*(b, \phi, \psi)}{\partial \epsilon_i^*} \frac{\partial E(b, \phi, \psi)}{\partial \epsilon_j} \, \mathrm{d}\phi \, \mathrm{d}\psi. \tag{3.3}$$

The differentiated field, or sensitivity field, satisfy Maxwell's equations (2.1)

$$\begin{cases} \nabla \times \frac{\partial \boldsymbol{E}}{\partial \epsilon_i} + \mathrm{i}k_0 \eta \frac{\partial \boldsymbol{H}}{\partial \epsilon_i} = \boldsymbol{0} \\ \nabla \times \frac{\partial \boldsymbol{H}}{\partial \epsilon_i} - \mathrm{i}\frac{k_0}{\eta} \epsilon \frac{\partial \boldsymbol{E}}{\partial \epsilon_i} = \mathrm{i}\frac{k_0}{\eta} \chi_i \boldsymbol{E} \end{cases} \tag{3.4}$$

as well as the wave equation (2.2)

$$\mathcal{L}\frac{\partial E}{\partial \epsilon_i} = \left\{ \frac{1}{\rho} \frac{\partial}{\partial \rho} \rho \frac{\partial}{\partial \rho} + \frac{1}{\rho^2} \frac{\partial^2}{\partial \phi^2} + k^2 \right\} \frac{\partial E}{\partial \epsilon_i} = -k_0^2 \chi_i E \tag{3.5}$$

where the solution E of (2.1) and (2.2) now appears in the source term $-k_0^2 \chi_i E$. The sensitivity field can hence be expressed as

$$\frac{\partial E(b, \phi, \psi)}{\partial \epsilon_i} = k_0^2 \int_{\mathcal{S}} G(\boldsymbol{\rho}, \boldsymbol{\rho}') \chi_i(\boldsymbol{\rho}') E(\boldsymbol{\rho}') \, \mathrm{d}S' = k_0^2 \int_{\mathcal{S}_i} G(\boldsymbol{\rho}, \boldsymbol{\rho}') E(\boldsymbol{\rho}') \, \mathrm{d}S'$$

$$= -\mathrm{i}k_0^3 \eta \int_{\mathcal{S}_i} G(b, \phi, \rho', \phi') G(b, \psi, \rho', \phi') \, \mathrm{d}S' \quad (3.6)$$

where we have employed the symmetry of the Greens function $G(\boldsymbol{\rho}, \boldsymbol{\rho}') = G(\boldsymbol{\rho}', \boldsymbol{\rho})$. Taking the two-dimensional Fourier transform of (3.6) we get the differentiated Fourier coefficients

$$\frac{\partial \widetilde{E}_{mn}(b)}{\partial \epsilon_i} = -\mathrm{i}k_0^3 \eta \int_{\mathcal{S}_i} \widetilde{G}_m(b, \rho', \phi') \widetilde{G}_n(b, \rho', \phi') \, \mathrm{d}S'. \tag{3.7}$$

The expression (3.7) can be greatly simplified by exploiting the symmetry properties of the Greens function corresponding to the homogenous and circularly symmetrical background, see the appendix. Hence, by using $\widetilde{G}_m(\rho, \rho', \phi') = \widetilde{G}_m(\rho, \rho', 0)\mathrm{e}^{-\mathrm{i}m\phi'}$ we get

$$\frac{\partial \widetilde{E}_{mn}(b)}{\partial \epsilon_i} = -\mathrm{i}k_0^3 \eta \int_{\mathcal{S}_i} \widetilde{G}_m(b, \rho', 0) \widetilde{G}_n(b, \rho', 0) \mathrm{e}^{-\mathrm{i}(m+n)\phi'} \, \mathrm{d}S' \tag{3.8}$$

displaying the significant quantity $\widetilde{G}_m(b, \rho', 0)$. Furthermore, by considering (3.6) and assuming that the pixel $\mathcal{S}_i$ is rotated an angle $\Delta\phi_i$ with respect to the pixel $\mathcal{S}_{i_0}$, we obtain the rotational invariance

$$\frac{\partial E(b, \phi + \Delta\phi_i, \psi + \Delta\phi_i)}{\partial \epsilon_i} = \frac{\partial E(b, \phi, \psi)}{\partial \epsilon_{i_0}} \tag{3.9}$$

and hence

$$\frac{\partial \widetilde{E}_{mn}(b)}{\partial \epsilon_i} = \frac{\partial \widetilde{E}_{mn}(b)}{\partial \epsilon_{i_0}} e^{-\mathrm{i}(m+n)\Delta\phi_i}. \tag{3.10}$$

These properties clearly indicate the simplifications that can be made in the modelling of the Fisher information matrix when the object as well as the discretization are circularly symmetrical.

3.2 Circularly Symmetrical Discretization

In order to get a rotational invariant definition of the resolution we employ a circularly symmetrical calculation grid with $N_\rho \times N_\phi$ grid points in the ρ and ϕ directions, respectively. In order to decimate the calculation grid for efficient calculation of the Cramér-Rao bound corresponding to a particular resolution, we chose N_ρ and N_ϕ to contain as many factors as possible, e.g., $N_\rho = p4!$ and $N_\phi = 6N_\rho$ ($\approx 2\pi N_\rho$) where p is an integer. The pixel grid is then defined by $n_\rho \times n_\phi$ points, where $n_\rho = N_\rho/q$, $n_\phi = N_\phi/q$ and q is the decimation factor.

The calculation grid is uniform in the ϕ-direction with increments $\Delta\phi = 2\pi/N_\phi$ whereas it is non-uniform in the ρ-direction. The circularly symmetrical unit cells are defined to have the same area $\Delta A = \pi r^2/(N_\rho N_\phi)$ where r is the radius of the circular domain under consideration. The radius r_n of the outher boundary of any unit cell is given by $r_n = \sqrt{\frac{2n\Delta A}{\Delta\phi}}$ for $n = 1, \ldots, N_\rho$ where $r_{N_\rho} = r$. The radial grid points ρ_n are defined by the center of gravity of the unit cells, yielding

$$\rho_n = 2\sin(\frac{\Delta\phi}{2})\frac{r_n^3 - r_{n-1}^3}{3}\frac{1}{\Delta A} \tag{3.11}$$

for $n = 1, \ldots, N_\rho$ and where $r_{-1} = 0$.

The pixel grid is defined in the same way as the calculation grid with $\Delta A_0 = \pi a^2/(n_\rho n_\phi)$, and we define the resolution parameter r_Δ by

$$r_\Delta = \frac{\sqrt{A_0}}{\lambda} \tag{3.12}$$

where $\lambda = 2\pi/\operatorname{Re}\{k\}$ is the wavelength inside the cylinder. Observe that the pixels are circularly symmetrical in the sense that one can be rotated into another, see Figure 4 for an example.

The Fourier coefficients of the sensitivity field (3.7) can now be efficiently calculated by approximating the integral in (3.8) by a summation over an offset pixel $\mathcal{S}_{i_0}$ and by employing the rotational invariance (3.10). Hence, let $\frac{\partial \widetilde{E}_{mn}}{\partial \epsilon_0}$ denote the $n_\rho \times 1$ vector containing pixel samples of (3.8) at an offset radial direction and let $\Delta\phi = 2\pi/n_\phi$ be the angular resolution on the pixel grid. The $n_\rho n_\phi \times n_\rho n_\phi$ Fisher information matrix (3.2) is then given by

$$\boldsymbol{\mathcal{I}} = \frac{1}{\sigma_\mathrm{N}^2} \sum_{m=-\infty}^{\infty} \sum_{n=-\infty}^{\infty} \boldsymbol{\Phi}_{mn} \otimes \left(\frac{\partial \widetilde{E}_{mn}}{\partial \epsilon_0}\right)^* \left(\frac{\partial \widetilde{E}_{mn}}{\partial \epsilon_0}\right)^{\mathrm{T}} \tag{3.13}$$

where $\mathbf{\Phi}_{mn}$ is an $n_\phi \times n_\phi$ matrix containing the elements $e^{i(m+n)(i-j)\Delta\phi}$ for $i, j = 1, \ldots, n_\phi$, $\otimes$ denotes the Kronecker product and $(\cdot)^{\mathrm{T}}$ the transpose. It is observed that the Fisher information matrix $\mathcal{I}$ has a block Toeplitz structure.

The Cramér-Rao bound (CRB) [12] for estimating the complex parameter ϵ_i is finally given by

$$\mathcal{E}\left\{|\widehat{\epsilon}_i - \epsilon_i|^2\right\} \geq \left[\mathcal{I}^{-1}\right]_{ii}. \tag{3.14}$$

The usefulness of the CRB with nonlinear problems is strongly motivated by the asymptotic properties of the Maximum Likelihood (ML) estimator [12]. Thus, assuming very general regularity conditions on the noise statistics, the ML estimate is asymptotically Gaussian distributed (for large data records) with an asymptotic error covariance equal to the CRB. Hence, the ML estimator is said to be *asymptotically efficient* and the CRB is *asymptotically achievable, cf.,* [12] for further details.

3.3   Cramér-Rao bound, accuracy and resolution

Next, we define an optimum trade-off between the accuracy and the resolution based on the Cramér-Rao bound and discuss how it can be used to asses a practical resolution limit in the inverse problem. In many respects, the idea resembles the concept of the *number of degrees of freedom* (NDF) of a linear operator, which is a useful tool in inverse scattering applications, see *e.g.,* [1, 2, 22]. The NDF, which is virtually independent of the noise level, can be used to estimate the number of retrievable parameters of an object, and hence the resolution. Typically, the NDF is defined as the number of significant singular values of a linear operator up to the point where their behaviour changes from "almost constant" to "exponentially decaying". For an inverse source problem with a simple cylindrical or spherical geometry, this property is closely related to the behaviour of the cylindrical or spherical Bessel and Hankel functions at the transition from evanescent to propagating regions, see *e.g.,* [1, 2, 22]. However, the NDF approaches are rather coarse and do not give a qualitative measure on the information content of the inversion data with respect to the accuracy and the resolution of images. In contrast, the Cramér-Rao bound is a performance measure which is qualitatively related to the information content of the inversion data.

The Cramér-Rao bound can be used to define an optimum trade-off between the accuracy and the resolution which is useful for linear as well as for nonlinear inverse problems. Hence, when the resolution of an imaging system is improved by decreasing the resolution parameter r_Δ, the corresponding accuracy in a given measurement set-up is impaired in the sense that the Cramér-Rao bound is increased. Formally, we may define the optimum trade-off between the accuracy and the resolution by the performance measure $\mathrm{PM}(r_\Delta)$

$$\begin{cases} \mathrm{PM}(r_\Delta) = \max_i \left[\mathcal{I}^{-1}\right]_{ii} \\ r_\Delta \text{ fixed} \end{cases} \tag{3.15}$$

where the maximization is taken over all pixels. Note that the resolution parameter r_Δ defines the number of pixels and hence the number of retrieved parameters.
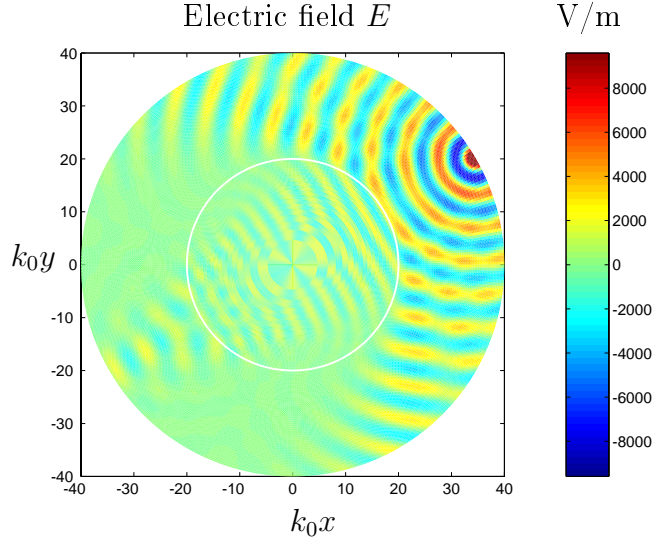
Figure 2: Illustration of the Greens function at external excitation. The electrical size of the object cylinder is $k_0 a = 20$, the measurement cylinder radius is $b = 2.0a$ and the background parameters are $\epsilon = 3 - i0.1$.

Precisely as is the case with the NDF for linear operators, the relation (3.15) will in many cases show a very sharp "knee" as the resolution parameter r_Δ decreases. The point at which this occur, *i.e.*, the point at which the Cramér-Rao bound starts to increase excessively, may be taken as the resolution limit of the imaging system. It will be possible, but clearly very impractical to estimate parameters beyond the resolution limit. Hence, the Cramér-Rao bound and the relation (3.15) can be used as an alternative definition of the "number of degrees of freedom" of a nonlinear inverse problem.

Eventhough the definition of the resolution limit based on the Cramér-Rao bound as described above is not precise unless we exactly specify the "knee" at which the Cramér-Rao bound starts to increase excessively, the optimum trade-off (3.15) is a useful tool for investigating the main characteristics of a given inverse problem with respect to the accuracy and the resolution. Moreover, the Cramér-Rao bound is a precise measure of accuracy, and is hence very useful for comparison studies such as *e.g.*, when investigating the effect (loss or gain in performance) of varying the measurement radius b (near-field effects), the operating frequency (electrical size $k_0 a$) or losses (complex permittivity ϵ). Numerical examples which illustrate the analysis procedure are given in the next section .

4 Numerical examples

The numerical examples described below illustrate how the Fisher information analysis can be used to investigate the significance of measurement distance, operating frequency and losses in a canonical two-dimensional microwave tomography set-up. In the numerical examples below, we have employed two electrical sizes of the object
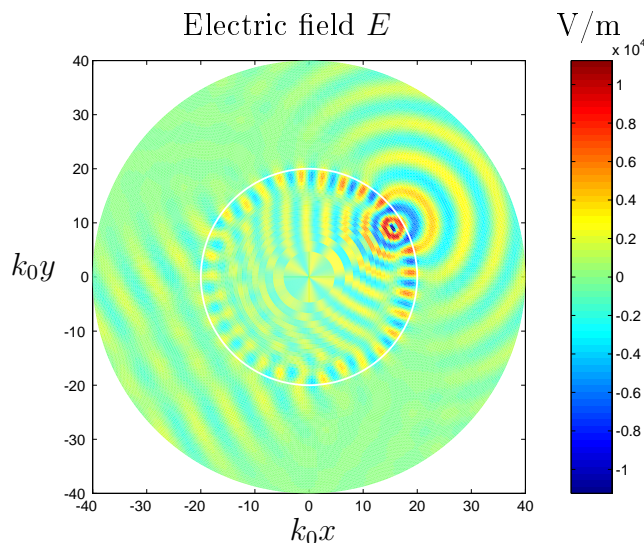
Figure 3: Illustration of the Greens function at internal excitation. The electrical size of the object cylinder is $k_0a = 20$, the measurement cylinder radius is $b = 2.0a$ and the background parameters are $\epsilon = 3 - i0.1$.

cylinder corresponding to $k_0a \in \{5, 20\}$, three radii b of the measurement cylinder $b \in \{1.1a, 1.5a, 2.0a\}$ and four different loss levels corresponding to the background parameters $\epsilon = \epsilon' - i\epsilon''$ where $\epsilon' = 3$ and $\epsilon'' \in \{0, 0.1, 0.3, 1\}$ In Figure 2–5 described below, the background parameters are $\epsilon = 3 - i0.1$. In order to get a fair comparison of the different measurement conditions (distance, frequency and loss), we employ the same signal-to-noise ratio SNR = 0 dB in all examples below.

Figure 2 and 3 illustrate the external and internal Greens functions at a calculation grid consisting of $N_\rho \times N_\phi = 72 \times 432 = 31104$ grid points corresponding to a resolution parameter $r_\Delta = 0.11$ inside the cylinder. The electrical size of the object cylinder is $k_0a = 20$ and the radius of the measurement cylinder is $b = 2.0a$. Wave scattering phenomena such as diffraction, interference patterns etc., are clearly visible. Note, however, that the apparent distortion close to the origin is due to the discretization in a case where the pixels become extremely thin. In Figure 4 is illustrated the corresponding Cramér-Rao bound (3.14) for pixels inside the object cylinder with the resolution parameter $r_\Delta = 0.33$. Figure 4 also illustrates the geometry of the circularly symmetrical pixels having equal area and varying radial dimension. Obviously, it is much harder to estimate pixels in the interior of the object in comparison to the outer boundary, particularly in the case where there are losses. In order to get good estimation performance, wave energy must be allowed to propagate from the transmitter to the pixel as well as from the pixel to the receiver without excessive loss.

Figure 5 displays the rapid decay of the Fourier coefficients $\widetilde{G}_m(b, \rho', 0)$ when the object cylinder electrical size is $k_0a = 20$, measurement cylinder radius $b \in \{1.1a, 2.0a\}$ and source positions at $k_0\rho' \in \{1.6, 10.1, 19.9\}$ (center, intermediate, surface). In the calculation of (3.14), we have employed as many Fourier coefficients
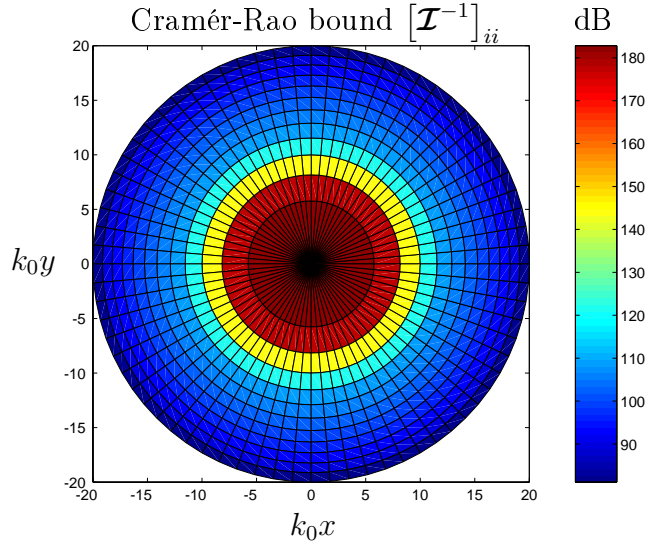
Figure 4: Cramér-Rao bound for pixels with resolution parameter $r_\Delta = 0.33$. The electrical size of the object cylinder is $k_0 a = 20$, the measurement cylinder radius is $b = 2.0a$ and the background parameters are $\epsilon = 3 - i0.1$.

that we could retrieve with numerical stability. Figure 5 also illustrates how the higher order modes become active (and hence increase the information content) as the measurement cylinder is getting smaller.

Figure 6 shows the Cramér-Rao bound for pixels at different positions $k_0\rho$ and resolution parameters r_Δ. The electrical size of the object cylinder is $k_0 a = 20$, the measurement cylinder radius is $b = 2.0a$ and the background parameters are $\epsilon = 3 - i0.3$. In this case, we can see that the resolution parameter $r_\Delta = 0.33$ is clearly below the resolution limit due to the excessive Cramér-Rao bound implying poor estimation performance. Note also that the radial variation in the Cramér-Rao bound diminishes as the resolution parameter r_Δ is increased above the resolution limit.

Figure 7 shows the Cramér-Rao bound for pixels at different positions $k_0\rho$, resolution parameters r_Δ and measurement cylinder radius $b \in \{1.1a, 1.5a, 2.0a\}$. The electrical size of the object cylinder is $k_0 a = 20$ and the background parameters are $\epsilon = 3 - i0.3$. The figure clearly illustrates the near-field effect, *i.e.*, a significant improvement in the estimation performance for pixels close to the circular object boundary when the radius of the measurement cylinder is decreased.

Figure 8 shows the Cramér-Rao bound for pixels at different positions $k_0\rho$, resolution parameters r_Δ and background parameters $\epsilon = \epsilon' - i\epsilon''$ where $\epsilon' = 3$ and $\epsilon'' \in \{0, 0.1, 0.3\}$. The electrical size of the object cylinder is $k_0 a = 20$ and the measurement cylinder radius is $b = 1.1a$. This figure clearly illustrates the high losses in estimation performance that is associated with high dielectric losses ϵ''.

Figure 9 shows the Cramér-Rao bound ratio $\text{CRB}(b)/\text{CRB}(2.0a)$ relative to $b = 2.0a$ for pixels at different positions $k_0\rho$, resolution parameters $r_\Delta \in \{0.44, 0.50, 0.67\}$ and measurement cylinder radius $b \in \{1.1a, 1.5a\}$. The electrical size of the object
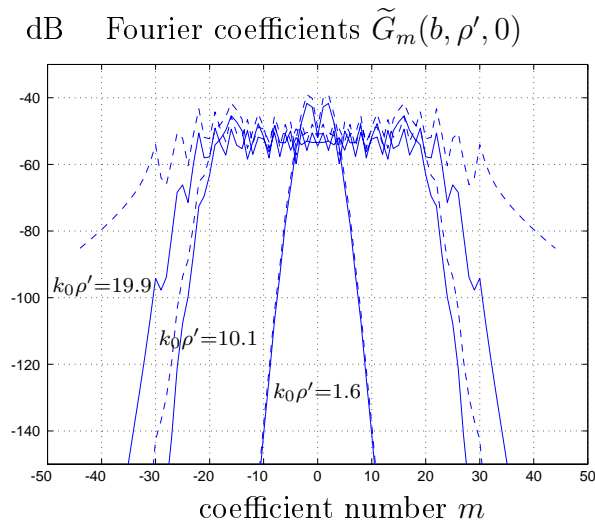
dB   Fourier coefficients $\widetilde{G}_m(b, \rho', 0)$

coefficient number m

Figure 5: Fourier coefficients $\widetilde{G}_m(b, \rho', 0)$ for source positions at $k_0\rho' \in \{1.6, 10.1, 19.9\}$. The electrical size of the object cylinder is $k_0 a = 20$, the measurement cylinder radius is $b = 2.0a$ (solid line) and $b = 1.1a$ (dashed line) and the background parameters are $\epsilon = 3 - \mathrm{i}0.1$.

cylinder is $k_0 a = 20$ and the background parameters are $\epsilon = 3 - \mathrm{i}0.3$. This figure clearly illustrates the near-field effect, *i.e.*, the relatively high gain in estimation performance that can be achieved when the measurement cylinder is close to the object. This effect is relatively independent of the resolution parameter r_Δ.

Figure 10 shows the Cramér-Rao bound ratio $\mathrm{CRB}(\epsilon)/\mathrm{CRB}(3)$ relative to $\epsilon = 3$ (lossless case) for pixels at different positions $k_0\rho$, resolution parameters $r_\Delta \in \{0.44, 0.50, 0.67\}$ and background parameters $\epsilon = \epsilon' - \mathrm{i}\epsilon''$ where $\epsilon' = 3$ and $\epsilon'' \in \{0.1, 0.3, 1\}$. The electrical size of the object cylinder is $k_0 a = 20$ and the measurement cylinder radius is $b = 1.1a$. This figure clearly illustrates the high losses in estimation performance that is associated with high dielectric losses ϵ''. This effect is relatively independent of the resolution parameter r_Δ.

Figure 11 shows the maximum Cramér-Rao bound (3.15) for pixels with different resolution parameters r_Δ. The electrical size of the object cylinder is $k_0 a \in \{5, 20\}$ and the radius of the measurement cylinder is $b \in \{1.1a, 1.5a, 2.0a\}$. The background parameters are $\epsilon = 3 - \mathrm{i}0.1$. In this example, we can see that the resolution limit in terms of the resolution parameter r_Δ is between 0.3 and 0.5 wavelengths, and that it is smaller when the electrical size of the object is smaller. This effect is relatively independent of the measurement distance b.

Figure 12 shows the maximum Cramér-Rao bound (3.15) for pixels with different resolution parameters r_Δ. The electrical size of the object cylinder is $k_0 a \in \{5, 20\}$ and the background parameters are $\epsilon = \epsilon' - \mathrm{i}\epsilon''$ where $\epsilon' = 3$ and $\epsilon'' \in \{0, 0.1, 0.3, 1\}$. The radius of the measurement cylinder is $b = 1.1a$. In this example, we can see again that the resolution limit in terms of the resolution parameter r_Δ is between 0.3 and 0.5 wavelengths, and that it is smaller when the electrical size of the object
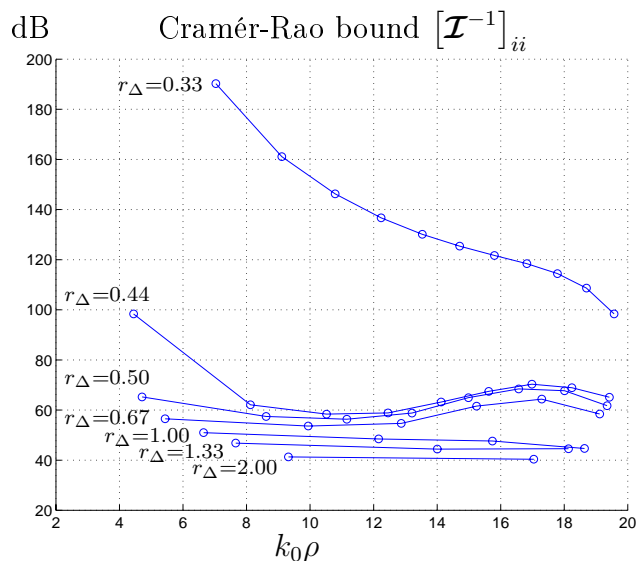
Figure 6: Cramér-Rao bound $\left[\mathcal{I}^{-1}\right]_{ii}$ for pixels at different positions $k_0\rho$ and resolution parameters r_Δ. The electrical size of the object cylinder is $k_0a = 20$, the measurement cylinder radius is $b = 2.0a$ and the background parameters are $\epsilon = 3 - \mathrm{i}0.3$.

is smaller. The effect is relatively independent of the loss parameter ϵ''. However, the "knee" determining the resolution limit tends to be less pronounced as the losses increase.

Finally, we conclude with an example where the losses are fixed and the real part of the relative permittivity is varied. Figure 13 shows the Cramér-Rao bound for pixels at different positions $k_0\rho$ and background parameters $\epsilon = \epsilon' - \mathrm{i}\epsilon''$ where $\epsilon'' = 0.1$ and $\epsilon' \in \{1, 1.5, 2, 2.5, 3\}$. The electrical size of the object cylinder is $k_0a = 20$ and the measurement cylinder radius is $b = 1.1a$. Note that the estimation performance is rapidly increasing (CRB decreasing) when ϵ' is increasing and $k_0\rho$ is small. This can be understood from a resolution limit perspective where the sequence $\epsilon' \in \{1, 1.5, 2, 2.5, 3\}$ corresponds to the increasing resolution parameters $r_\Delta \in \{0.29, 0.35, 0.41, 0.46, 0.5\}$, *cf.*, also Figure 6. Figure 14 shows the maximum Cramér-Rao bound (3.15) for pixels with different resolution parameters r_Δ. The electrical size of the object cylinder is $k_0a \in \{5, 20\}$ and the background parameters are $\epsilon = \epsilon' - \mathrm{i}\epsilon''$ where $\epsilon'' = 0.1$ and $\epsilon' \in \{1, 1.5, 2, 2.5\}$. The radius of the measurement cylinder is $b = 1.1a$. Note that the estimation performance as a function of the (wavelength normalized) resolution parameter r_Δ, does not depend significantly on ϵ'. However, for $k_0a = 5$, we can see very clearly that the effect of increasing ϵ' is very similar to the effect of increasing the frequency (decreasing the wavelength).

5   Summary and conclusions

We have presented a general framework for sensitivity analysis which is useful for establishing some important physical performance bounds in microwave tomography. As a canonical problem, the two-dimensional electromagnetic inverse problem
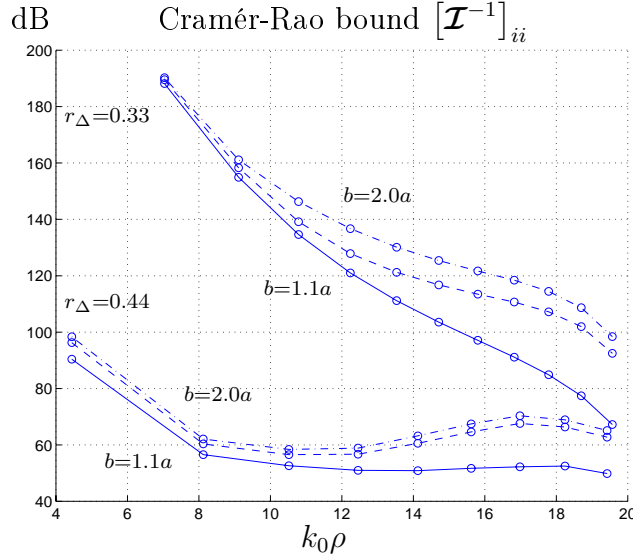
Figure 7: Cramér-Rao bound $\left[\boldsymbol{\mathcal{I}}^{-1}\right]_{ii}$ for pixels at different positions $k_0\rho$, resolution parameters r_Δ and measurement cylinder radius b. Here, $b = 1.1a$ (solid line), $b = 1.5a$ (dashed line) and $b = 2.0a$ (dashdotted line). The electrical size of the object cylinder is $k_0a = 20$ and the background parameters are $\epsilon = 3 - \mathrm{i}0.3$.

of imaging a cylinder with isotropic dielectric losses is considered. A fixed resolution is analyzed by introducing a finite basis, *i.e.*, pixels representing the material properties. The corresponding Cramér-Rao bound for estimating the pixel values is computed based on a calculation of the *sensitivity field* which is obtained by differentiating the observed field with respect to the estimated parameter. An optimum trade-off between the accuracy and the resolution is defined based on the Cramér-Rao bound, and its application to asses a practical resolution limit in the inverse problem is discussed. Hence, when the resolution of an imaging system is improved, the corresponding estimation accuracy in a given measurement set-up is impaired in the sense that the Cramér-Rao bound is increased. Numerical examples are included to illustrate how the Fisher information analysis can be used to investigate the significance of measurement distance, operating frequency and losses in the canonical tomography set-up. Hence, the Cramér-Rao bound can be used to quantitatively characterize the gain in estimation performance that is associated with a decrease in the measurement distance (the near-field effect) as well as a decrease in the dielectric losses, all at a fixed signal-to-noise ratio. Furthermore, the results show that a decrease in the operating frequency may in fact improve the resolution limit normalized to the wavelength. Finally, in an example where the losses are fixed and the real part of the relative permittivity is increased, it is illustrated how the corresponding increase in estimation performance can bee understood from a resolution limit perspective.
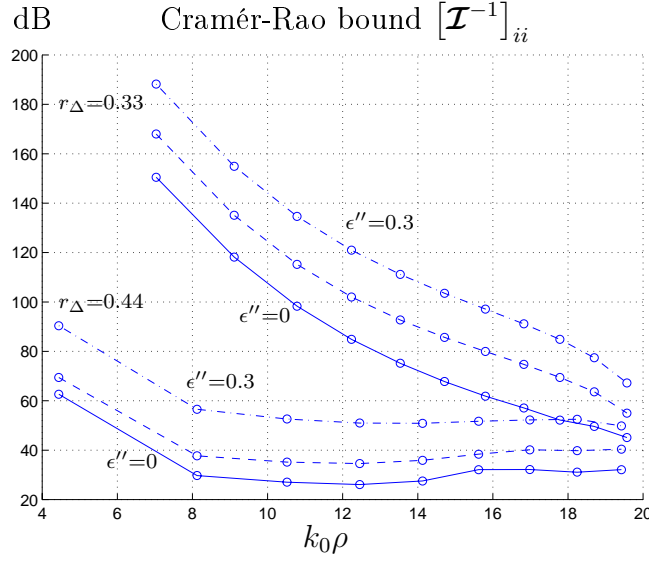
Figure 8: Cramér-Rao bound $\left[\boldsymbol{\mathcal{I}}^{-1}\right]_{ii}$ for pixels at different positions $k_0\rho$, resolution parameters r_Δ and background parameters $\epsilon = \epsilon' - \mathrm{i}\epsilon'' = 3 - \mathrm{i}\epsilon''$. Here, $\epsilon'' = 0$ (solid line), $\epsilon'' = 0.1$ (dashed line) and $\epsilon'' = 0.3$ (dashdotted line). The electrical size of the object cylinder is $k_0 a = 20$ and the measurement cylinder radius is $b = 1.1a$.

Acknowledgement

Appendix A   Greens function for the homogenous cylinder

The Greens function for the homogenous and circularly symmetrical background satisfies the scalar wave equation $\mathcal{L}G(\boldsymbol{\rho}, \boldsymbol{\rho}') = -\delta(\boldsymbol{\rho} - \boldsymbol{\rho}')$, or

$$\left\{ \frac{1}{\rho}\frac{\partial}{\partial\rho}\rho\frac{\partial}{\partial\rho} + \frac{1}{\rho^2}\frac{\partial^2}{\partial\phi^2} + k^2 \right\} G(\rho,\phi,\rho',\phi') = -\frac{\delta(\rho-\rho')}{\rho}\delta(\phi-\phi') \tag{A.1}$$

together with appropriate boundary conditions. By introducing the Fourier series expansion

$$G(\rho,\phi,\rho',\phi') = \sum_{m=-\infty}^{\infty} \widetilde{G}_m(\rho,\rho',\phi')\mathrm{e}^{\mathrm{i}m\phi} \tag{A.2}$$

the wave equation (A.1) transforms to

$$\left\{ \frac{1}{\rho}\frac{\partial}{\partial\rho}\rho\frac{\partial}{\partial\rho} + k^2 - \frac{m^2}{\rho^2} \right\} \widetilde{G}_m(\rho,\rho',\phi') = -\frac{\delta(\rho-\rho')}{\rho}\frac{\mathrm{e}^{-\mathrm{i}m\phi'}}{2\pi}. \tag{A.3}$$

dB   Cramér-Rao bound ratio CRB(b)/CRB($2.0a$)

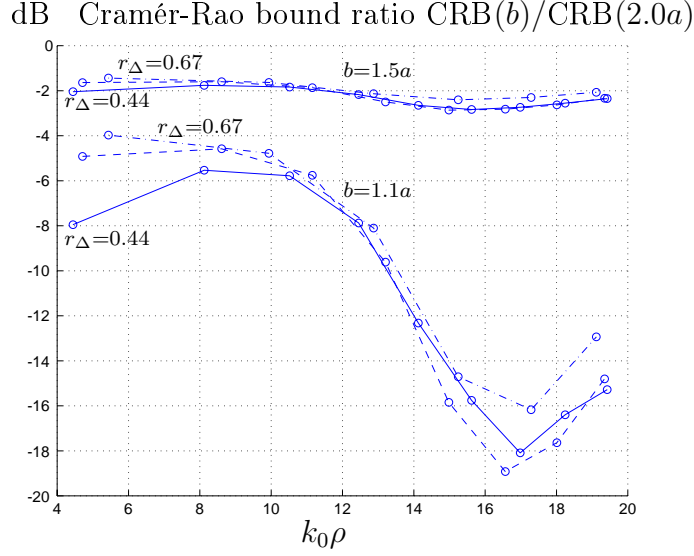**Figure 9**: Cramér-Rao bound ratio CRB(b)/CRB($2.0a$) relative to $b = 2.0a$ for pixels at different positions $k_0\rho$, resolution parameters r_Δ and measurement cylinder radius b. Here, $b = 1.1a$ and $b = 1.5a$, respectively, and the resolution parameter is $r_\Delta = 0.44$ (solid line), $r_\Delta = 0.50$ (dashed line) and $r_\Delta = 0.67$ (dashdotted line). The electrical size of the object cylinder is $k_0a = 20$ and the background parameters are $\epsilon = 3 - i0.3$.

Assume that the source is within the cylinder, *i.e.*, $\rho' < a$. The solution to (A.3) is then given by

$$\widetilde{G}_m(\rho, \rho', \phi') = \begin{cases} A_m \mathrm{J}_m(k\rho) & 0 < \rho < \rho' \\ B_m \mathrm{H}_m^{(1)}(k\rho) + C_m \mathrm{H}_m^{(2)}(k\rho) & \rho' < \rho < a \\ D_m \mathrm{H}_m^{(2)}(k_0\rho) & \rho > a \end{cases} \tag{A.4}$$

where J_m, $\mathrm{H}_m^{(1)}$ and $\mathrm{H}_m^{(2)}$ are the Bessel function and the Hankel functions of the first and second kind, respectively, all of order m. The appropriate boundary conditions related to the tangential fields $\boldsymbol{E}_\parallel$ and $\boldsymbol{H}_\parallel$ are given by

$$\begin{cases} \widetilde{G}_m(\rho'_+, \rho', \phi') - \widetilde{G}_m(\rho'_-, \rho', \phi') = 0 \\ \frac{\partial}{\partial\rho}\widetilde{G}_m(\rho'_+, \rho', \phi') - \frac{\partial}{\partial\rho}\widetilde{G}_m(\rho'_-, \rho', \phi') = -\frac{1}{\rho'}\frac{\mathrm{e}^{-im\phi'}}{2\pi} \\ \widetilde{G}_m(a_+, \rho', \phi') - \widetilde{G}_m(a_-, \rho', \phi') = 0 \\ \frac{\partial}{\partial\rho}\widetilde{G}_m(a_+, \rho', \phi') - \frac{\partial}{\partial\rho}\widetilde{G}_m(a_-, \rho', \phi') = 0 \end{cases} \tag{A.5}$$

where the arguments ρ_+ and ρ_- denotes a limit to ρ from the right and left, respec-

dB   Cramér-Rao bound ratio CRB(ϵ)/CRB(3)

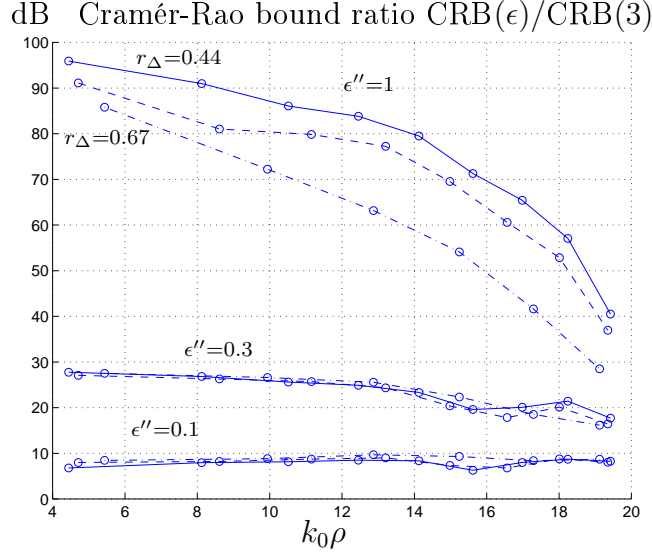**Figure 10**: Cramér-Rao bound ratio CRB(ϵ)/CRB(3) relative to $\epsilon = 3$ (lossless case) for pixels at different positions $k_0\rho$, resolution parameters r_Δ and background parameters $\epsilon = \epsilon' - \mathrm{i}\epsilon'' = 3 - \mathrm{i}\epsilon''$. Here, $\epsilon'' = 0.1$, $\epsilon'' = 0.3$ and $\epsilon'' = 1$, respectively, and the resolution parameter is $r_\Delta = 0.44$ (solid line), $r_\Delta = 0.50$ (dashed line) and $r_\Delta = 0.67$ (dashdotted line). The electrical size of the object cylinder is $k_0 a = 20$ and the measurement cylinder radius is $b = 1.1a$.

tively. The boundary conditions (A.5) yield the linear system of equations

$$
\begin{pmatrix}
-\mathrm{J}_m(k\rho') & \mathrm{H}_m^{(1)}(k\rho') & \mathrm{H}_m^{(2)}(k\rho') & 0 \\
-k\mathrm{J}_m'(k\rho') & k\mathrm{H}_m^{(1)'}(k\rho') & k\mathrm{H}_m^{(2)'}(k\rho') & 0 \\
0 & -\mathrm{H}_m^{(1)}(ka) & -\mathrm{H}_m^{(2)}(ka) & \mathrm{H}_m^{(2)}(k_0 a) \\
0 & -k\mathrm{H}_m^{(1)'}(ka) & -k\mathrm{H}_m^{(2)'}(ka) & k_0\mathrm{H}_m^{(2)'}(k_0 a)
\end{pmatrix}
$$
$$
\times \begin{pmatrix} A_m \\ B_m \\ C_m \\ D_m \end{pmatrix} = \begin{pmatrix} 0 \\ -\frac{1}{\rho'} \frac{\mathrm{e}^{-\mathrm{i}m\phi'}}{2\pi} \\ 0 \\ 0 \end{pmatrix} \quad \text{(A.6)}
$$

which is solved for the constants A_m, B_m, C_m and D_m defined in (A.4).

Assume now that the source is outside the cylinder, *i.e.*, $\rho' > a$. The solution to (A.3) is then given by

$$
\widetilde{G}_m(\rho, \rho', \phi') = \begin{cases} A_m\mathrm{J}_m(k\rho) & 0 < \rho < a \\ B_m\mathrm{H}_m^{(1)}(k_0\rho) + C_m\mathrm{H}_m^{(2)}(k_0\rho) & a < \rho < \rho' \\ D_m\mathrm{H}_m^{(2)}(k_0\rho) & \rho > \rho'. \end{cases} \quad \text{(A.7)}
$$

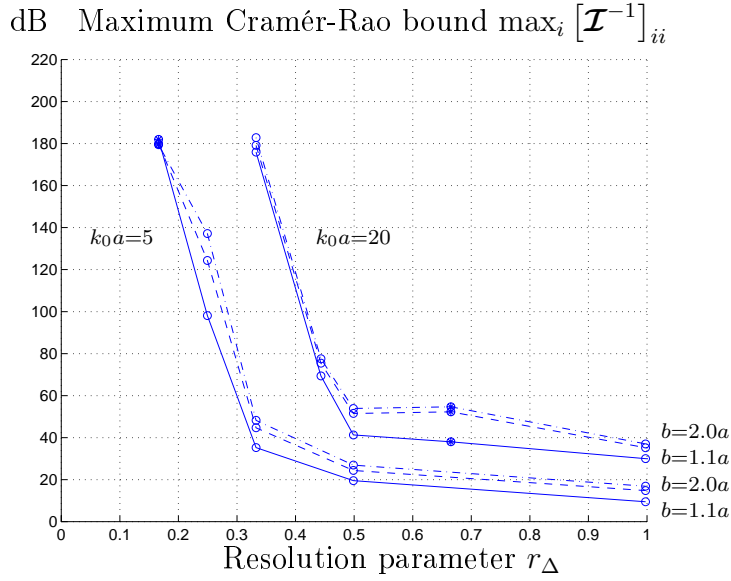The appropriate boundary conditions related to the tangential fields $\boldsymbol{E}_\parallel$ and $\boldsymbol{H}_\parallel$ are

Figure 11: Maximum Cramér-Rao bound $\max_i \left[\boldsymbol{\mathcal{I}}^{-1} \right]_{ii}$ for pixels with different resolution parameters r_Δ. The electrical size of the object cylinder is $k_0 a = 5$ and $k_0 a = 20$, respectively, and the radius of the measurement cylinder is $b = 1.1a$ (solid line), $b = 1.5a$ (dashed line) and $b = 2.0a$ (dashdotted line). The background parameters are $\epsilon = 3 - i0.1$.

now given by

$$
\begin{cases}
\widetilde{G}_m(a_+, \rho', \phi') - \widetilde{G}_m(a_-, \rho', \phi') = 0 \\
\frac{\partial}{\partial \rho} \widetilde{G}_m(a_+, \rho', \phi') - \frac{\partial}{\partial \rho} \widetilde{G}_m(a_-, \rho', \phi') = 0 \\
\widetilde{G}_m(\rho'_+, \rho', \phi') - \widetilde{G}_m(\rho'_-, \rho', \phi') = 0 \\
\frac{\partial}{\partial \rho} \widetilde{G}_m(\rho'_+, \rho', \phi') - \frac{\partial}{\partial \rho} \widetilde{G}_m(\rho'_-, \rho', \phi') = -\frac{1}{\rho'} \frac{e^{-im\phi'}}{2\pi}.
\end{cases}
\tag{A.8}
$$

The boundary conditions (A.8) yield the linear system of equations

$$
\begin{pmatrix}
-\mathrm{J}_m(ka) & \mathrm{H}_m^{(1)}(k_0 a) & \mathrm{H}_m^{(2)}(k_0 a) & 0 \\
-k\mathrm{J}_m'(ka) & k_0\mathrm{H}_m^{(1)\prime}(k_0 a) & k_0\mathrm{H}_m^{(2)\prime}(k_0 a) & 0 \\
0 & -\mathrm{H}_m^{(1)}(k_0 \rho') & -\mathrm{H}_m^{(2)}(k_0 \rho') & \mathrm{H}_m^{(2)}(k_0 \rho') \\
0 & -k_0\mathrm{H}_m^{(1)\prime}(k_0 \rho') & -k_0\mathrm{H}_m^{(2)\prime}(k_0 \rho') & k_0\mathrm{H}_m^{(2)\prime}(k_0 \rho')
\end{pmatrix}
$$
$$
\times
\begin{pmatrix}
A_m \\
B_m \\
C_m \\
D_m
\end{pmatrix}
=
\begin{pmatrix}
0 \\
0 \\
0 \\
-\frac{1}{\rho'} \frac{e^{-im\phi'}}{2\pi}
\end{pmatrix}
\tag{A.9}
$$

which is solved for the constants A_m, B_m, C_m and D_m defined in (A.7). Note that the circular symmetry implies that $\widetilde{G}_m(\rho, \rho', \phi') = \widetilde{G}_m(\rho, \rho', 0)e^{-im\phi'}$ for both cases above.
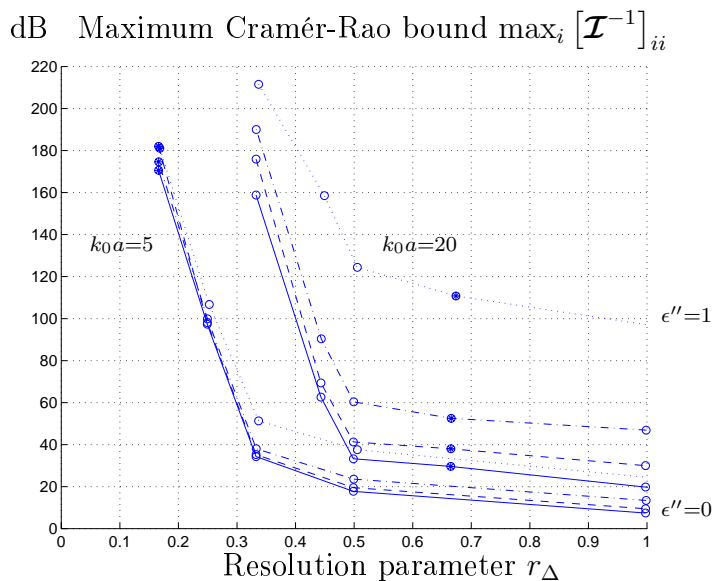
Figure 12: Maximum Cramér-Rao bound $\max_i \left[\boldsymbol{\mathcal{I}}^{-1}\right]_{ii}$ for pixels with different resolution parameters r_Δ. The electrical size of the object cylinder is $k_0 a = 5$ and $k_0 a = 20$, respectively, and the background parameters are $\epsilon = \epsilon' - \mathrm{i}\epsilon'' = 3 - \mathrm{i}\epsilon''$ where $\epsilon'' = 0$ (solid line), $\epsilon'' = 0.1$ (dashed line), $\epsilon'' = 0.3$ (dashdotted line) and $\epsilon'' = 1$ (dotted line). The radius of the measurement cylinder is $b = 1.1a$.

References

[1] M. Bertero. Linear inverse and ill–posed problems. *Advances in electronics and electron physics*, **75**, 1–120, 1989.

[2] O. M. Bucci, L. Crocco, T. Isernia, and V. Pascazio. Subsurface inverse scattering problems: Quantifying qualifying and achieving the available information. *IEEE Trans. Geoscience and Remote Sensing*, **39**(11), 2527–2538, November 2001.

[3] M. Cheney and D. Isaacson. Issues in electrical impedance imaging. *IEEE Computational Science & Engineering*, pages 53–62, 1995.

[4] S. L. Collier. Fisher information for a complex Gaussian random variable: Beamforming applications for wave propagation in a random medium. *IEEE Trans. Signal Process.*, **53**(11), 4236–4248, November 2005.

[5] D. Colton and R. Kress. *Inverse Acoustic and Electromagnetic Scattering Theory*. Springer-Verlag, Berlin, 1992.

[6] A. J. Devaney and G. A. Tsihirintzis. Maximum likelihood estimation of object location in diffraction tomography. *IEEE Trans. Signal Process.*, **39**(3), 672–682, March 1991.
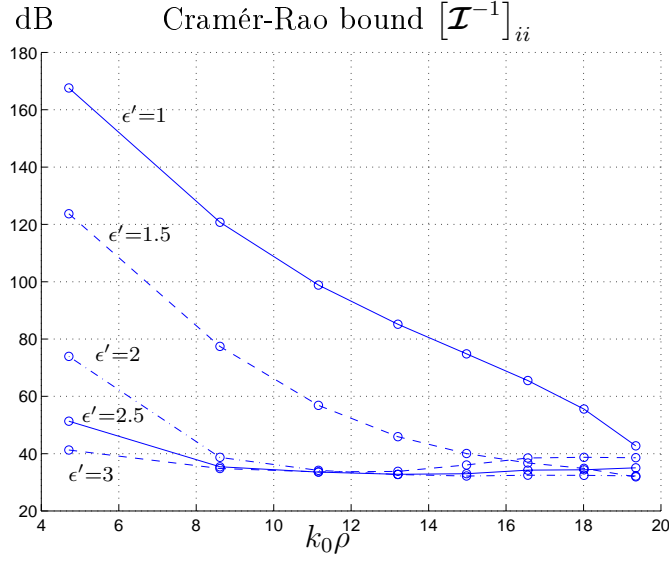
Figure 13: Cramér-Rao bound $\left[\boldsymbol{\mathcal{I}}^{-1}\right]_{ii}$ for pixels at different positions $k_0\rho$ and background parameters $\epsilon = \epsilon' - \mathrm{i}\epsilon'' = \epsilon' - \mathrm{i}0.1$. Here, $\epsilon' = 1$ (solid line), $\epsilon' = 1.5$ (dashed line), $\epsilon' = 2$ (dashdotted line), $\epsilon' = 2.5$ (solid line) and $\epsilon' = 3$ (dashed line). The electrical size of the object cylinder is $k_0 a = 20$ and the measurement cylinder radius is $b = 1.1a$.

[7] A. Dogandzic and A. Nehorai. Cramér–Rao bounds for estimating range, velocity, and direction with an active array. *IEEE Trans. Signal Process.*, **49**(6), 1122–1137, June 2001.

[8] A. Fhager and M. Persson. Comparison of two image reconstruction algorithms for microwave tomography. *Radio Sci.*, **40**(RS3017), June 2005.

[9] M. Gustafsson. *Wave Splitting in Direct and Inverse Scattering Problems*. PhD thesis, Lund Institute of Technology, Department of Electromagnetic Theory, P.O. Box 118, S-221 00 Lund, Sweden, 2000. http://www.es.lth.se/home/mats.

[10] M. Gustafsson and S. Nordebo. Cramér–Rao lower bounds for inverse scattering problems of multilayer structures. *Inverse Problems*, **22**, 1359–1380, 2006.

[11] V. Isakov. *Inverse Problems for Partial Differential Equations*. Springer-Verlag, Berlin, 1998.

[12] S. M. Kay. *Fundamentals of Statistical Signal Processing, Estimation Theory*. Prentice-Hall, Inc., NJ, 1993.

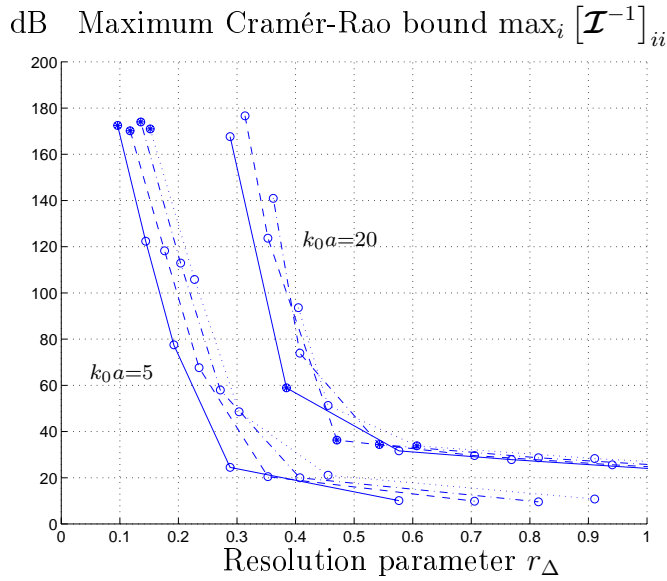[13] A. Kirsch. *An Introduction to the Mathematical Theory of Inverse Problems*. Springer-Verlag, New York, 1996.

Figure 14: Maximum Cramér-Rao bound $\max_i \left[\boldsymbol{\mathcal{I}}^{-1}\right]_{ii}$ for pixels with different resolution parameters r_Δ. The electrical size of the object cylinder is $k_0 a = 5$ and $k_0 a = 20$, respectively, and the background parameters are $\epsilon = \epsilon' - i\epsilon'' = \epsilon' - i0.1$ where $\epsilon' = 1$ (solid line), $\epsilon' = 1.5$ (dashed line), $\epsilon' = 2$ (dashdotted line) and $\epsilon' = 2.5$ (dotted line). The radius of the measurement cylinder is $b = 1.1a$.

[14] H. Krim and M. Viberg. Two decades of array signal processing research: the parametric approach. *IEEE Signal Processing Magazine*, **13**(4), 67–94, July 1996.

[15] E. A. Marengo and R. W. Ziolkowski. Nonradiating and minimum energy sources and their fields: Generalized source inversion theory and applications. *IEEE Trans. Antennas Propagat.*, **48**(10), 1553–1562, October 2000.

[16] K. S. Miller. *Complex Stochastic Processes*. Addison–Wesley Publishing Company, Inc., 1974.

[17] P. S. Naidu and A. Buvaneswari. A study of Cramér–Rao bounds on object shape parameters from scattered field. *IEEE Trans. Signal Process.*, **47**(5), 1478–1481, May 1999.

[18] B. Nilsson. 3D electromagnetic modelling for determination of pitch in twisted cylinders. In *AIP Conference Proceedings*, volume 834, pages 268–277. Växjö university, Sweden, 2006.

[19] B. Nilsson. Determination of pitch in twisted cylinders by electromagnetic scattering. *Wave Motion*, **43**(3), 259–271, 2006.

[20] S. Nordebo, M. Gustafsson, and K. Persson. Sensitivity analysis for antenna near-field imaging, 2006. To appear in IEEE Trans. Signal Process.

[21] S. Nordebo and M. Gustafsson. Statistical signal analysis for the inverse source problem of electromagnetics. *IEEE Trans. Signal Process.*, **54**(6), 2357–2361, June 2006.

[22] R. Pierri and F. Soldovieri. On the information content of the radiated fields in the near zone over bounded domains. *Inverse Problems*, **14**(2), 321–337, 1998.

[23] S. T. Smith. Statistical resolution limits and the complexified Cramér–Rao bound. *IEEE Trans. Signal Process.*, **53**(5), 1597–1609, May 2005.

[24] T. Söderström and P. Stoica. *System Identification.* Prentice-Hall, Inc., Englewood Cliffs, New Jersey, 2001.

[25] A. Tarantola. *Inverse problem theory and methods for model parameter estimation.* Society for Industrial and Applied Mathematics, Philadelphia, 2005.

[26] G. A. Tsihirintzis and A. J. Devaney. Maximum likelihood estimation of object location in diffraction tomography, Part II; strongly scattering objects. *IEEE Trans. Signal Process.*, **39**(6), 1466–1470, June 1991.